Single Semiconductor Nanostructure Extinction Spectroscopy

*Rusha Chatterjee, Ilia M. Pavlovetc, Kyle Aleshire, Masaru Kuno**

Department of Chemistry and Biochemistry, University of Notre Dame, 251 Nieuwland Science Hall, Notre Dame, Indiana 46556, United States

Supporting Information

Contents

1. Modeling absorption cross-sections S2
2. Tables of QD, NR and NW absorption cross-sections S3
3. Modeling the PHI signal S5
4. Experimental and theoretical Au NP extinction cross-sections S12
5. Conceptual illustration of SMS S13
6. Modeling the SMS signal through a Taylor series expansion S13
7. Modeling the SMS signal through a Fourier series expansion S15
8. SMS extinction spectra S16
9. Custom autobalanced photodetector S18

References S21

1. Modeling absorption cross-sections

The underlying idea behind **Equation 1** in the main text involves Maxwell Garnett effective medium theory[1,2], which models the effective (complex) dielectric constant $\left(\tilde{\varepsilon}_{eff} = \varepsilon_1' + i\varepsilon_2'\right)$ of a medium as that of a matrix with foreign inclusions embedded within it. For spherical inclusions with a volume fraction, *p*, Maxwell-Garnett shows that

$$\tilde{\varepsilon}_{eff} = \varepsilon_m \left[1 + \frac{3p\left(\frac{\tilde{\varepsilon}_s(\omega)-\varepsilon_m}{\tilde{\varepsilon}_s(\omega)+2\varepsilon_m}\right)}{1-p\left(\frac{\tilde{\varepsilon}_s(\omega)-\varepsilon_m}{\tilde{\varepsilon}_s(\omega)+2\varepsilon_m}\right)}\right] \tag{S1}$$

where ε_m is the dielectric constant of the matrix, assumed to be real, and $\tilde{\varepsilon}_s(\omega) = \varepsilon_1 + i\varepsilon_2$ is the complex dielectric constant of the semiconductor. In the limit p<<1, the imaginary part of the effective medium's dielectric constant is

$$\varepsilon_2' = 9p\varepsilon_m^2 \frac{\varepsilon_2}{(\varepsilon_1+2\varepsilon_m)^2+\varepsilon_2^2}. \tag{S2}$$

Equation S2 is, in turn, linked to the medium's extinction coefficient, κ', via $\kappa' = \frac{\varepsilon_2'}{2n'}$ where n' is the real part of the medium's complex refractive index. What results is

$$\kappa' = \frac{p}{2n'}|f(\omega)|^2\varepsilon_2 \tag{S3}$$

with $f(\omega) = \frac{3\varepsilon_m}{\tilde{\varepsilon}_s(\omega)+2\varepsilon_m}$ being the local field factor for the spherical inclusion. By relating κ' to the medium's absorption coefficient via $\alpha' = \frac{2\omega k'}{c}$ and by using the relationship $\varepsilon_2 = 2n_s k_s$ as well as by assuming that $n' \approx n_m$, with $n_m$the refractive index of the matrix, we find

$$\alpha' = \frac{\omega}{n_m c} p|f(\omega)|^2 2n_s k_s. \tag{S4}$$

Equation S4 can be expressed in terms of the cross section (σ) as $\alpha' = C\sigma(\omega)$ where $C = \frac{N}{V_{tot}}$ is the number density of inclusions in the matrix, expressed in terms of *N*, the absolute number of

inclusions and V_{tot}, the total volume of the matrix. Since $p = \frac{NV}{V_{tot}}$, where V is the volume of an individual inclusion, the desired absorption cross section of the spherical particle is

$$\sigma(\omega) = \frac{\omega}{n_m c} V \left| \frac{3\varepsilon_m}{\tilde{\varepsilon}_s(\omega) + 2\varepsilon_m} \right|^2 (2 n_s k_s) \tag{S5}$$

with $V = \frac{4}{3}\pi a^3$ and a the particle's radius. This is **Equation 2** of the main text.

2. Tables of QD, NR, and NW absorption cross-sections

Table S1. Compilation of semiconductor QD absorption cross sections.

System	Band edge molar extinction coefficient (M^{-1} cm^{-1})	Band edge absorption cross section (cm^2)	Molar extinction coefficient at other wavelengths (M^{-1} cm^{-1})	Absorption cross section at other wavelengths (cm^2)	Reference
ZnS	(*a*=1.0-1.8 nm) **2.9×10^{6}-6.3×10^{6}**	(*a*=1.0-1.8 nm) **1.1×10^{-14}-2.4×10^{-14}**			3
ZnSe	(*a*=1.4-2.4 nm) **8.6×10^{4}-2.4×10^{5}**	(*a*=1.4-2.4 nm) **3.3×10^{-16}-9.3×10^{-16}**			4
CdS	(*a*=0.65-4.8 nm) **8.0×10^{3}-7.4×10^{2}**	(*a*=0.65-4.8 nm) **3.0×10^{-17}-2.8×10^{-18}**			5
	(*a*=0.75-2.7 nm) **7.4×10^{4}-9.9×10^{5}**	(*a*=0.75-2.7 nm) **2.8×10^{-16}-3.8×10^{-15}**			6
	(*a*=2.3-2.7 nm) **6.8×10^{5}-1.1×10^{6}**	(*a*=2.3-2.7 nm) **2.6×10^{-15}-4.1×10^{-15}**			7
	(*a*=1.1-2.9 nm) **3.1×10^{5}-1.2×10^{6}**	(*a*=1.1-2.9 nm) **1.2×10^{-15}-4.7×10^{-15}**			8
$CsPbBr_3$	(*a*=3.8-5.5 nm) **9.2×10^{5}-3.4×10^{6}**	(*a*=3.8-5.5 nm) **3.5×10^{-15}-1.3×10^{-14}**			9
CdSe	(*a*=1.4-2.8 nm) **3.8×10^{5}-9.2×10^{5}**	(*a*=1.4-2.8 nm) **1.5×10^{-15}-3.5×10^{-15}**			4

	(*a*=0.65-2.6 nm) **$1.4x10^4$-$2.1x10^5$**	(*a*=0.65-2.6 nm) **$5.5x10^{-17}$-$8.0x10^{-16}$**			10
	(*a*=1.2-3.1 nm) **$2.8x10^5$-$1.2x10^6$**	(*a*=1.2-3.1 nm) **$1.0x10^{-15}$-$4.7x10^{-15}$**			11
	(*a*=1.1-3.1 nm) **$1.5x10^4$-$7.6x10^5$**	(*a*=1.1-3.1 nm) **$5.8x10^{-17}$-$2.9x10^{-15}$**			6
	(*a*=1.2-3.4 nm) **$1.7x10^5$-$9.7x10^5$**	(*a*=1.2-3.4 nm) **$6.4x10^{-16}$-$3.7x10^{-15}$**	(*a*=1.5-3.0 nm) **$4.6x10^5$-$4.0x10^6$** @350 nm	(*a*=1.5-3.0 nm) **$1.8x10^{-15}$-$1.5x10^{-14}$** @350 nm	12
	(*a*=1.0-2.8 nm) **$1.6x10^5$-$5.3x10^5$**	(*a*=1.0-2.8 nm) **$5.9x10^{-16}$-$2.0x10^{-15}$**			13
	(*a*=1.0-3.0 nm) **$2.2x10^4$-$4.7x10^4$**	(*a*=1.0-3.0 nm) **$8.5x10^{-17}$-$1.8x10^{-16}$**	(*a*=1.0-3.0 nm) **$1.1x10^5$-$2.9x10^6$** @400 nm	(*a*=1.0-3.0 nm) **$4.2x10^{-16}$-$1.1x10^{-14}$** @400 nm	14
$CuInS_2$	(*a*=1.3-2.9 nm) **$8.9x10^4$-$5.0x10^5$**	(*a*=1.3-2.9 nm) **$3.4x10^{-16}$-$1.9x10^{-15}$**			3
CdTe	(*a*=1.0-2.0 nm) **$4.5x10^3$-$1.1x10^3$**	(*a*=1.0-2.0 nm) **$1.7x10^{-17}$-$4.2x10^{-18}$**			15
	(*a*=1.7-3.5 nm) **$6.4x10^4$-$6.0x10^5$**	(*a*=1.7-3.5 nm) **$2.4x10^{-16}$-$2.3x10^{-15}$**			6
	(*a*=1.0-4.0 nm) **$8.2x10^2$-$1.4x10^6$**	(*a*=1.0-4.0 nm) **$3.1x10^{-18}$-$5.5x10^{-15}$**	(*a*=1.0-4.0 nm) **$8.9x10^4$-$5.7x10^6$** @400 nm	(*a*=1.0-4.0 nm) **$3.4x10^{-16}$-$2.2x10^{-14}$** @400 nm	14
InAs	(*a*=1.6-3.5 nm) **$1.7x10^5$-$4.0x10^5$**	(*a*=1.6-3.5 nm) **$6.4x10^{-16}$-$1.5x10^{-15}$**	(*a*=1.6-3.5 nm) **$4.7x10^5$-$6.0x10^6$** @450 nm	(*a*=1.6-3.5 nm) **$1.8x10^{-15}$-$2.3x10^{-14}$** @450 nm	16
PbS	(*a*=2.1-3.2 nm) **$1.0x10^5$-$3.0x10^5$**	(*a*=2.1-3.2 nm) **$4.0x10^{-16}$-$1.1x10^{-15}$**			17
PbSe	(*a*=1.6-2.7 nm) **$6.6x10^4$-$2.4x10^5$**	(*a*=1.6-2.7 nm) **$2.5x10^{-16}$-$9.2x10^{-16}$**			18

Table S2. Compilation of semiconductor NR and NW absorption cross sections.

System	Band edge absorption cross section (cm^2mm^{-1})	Absorption cross section at other wavelengths (cm^2mm^{-1})	Reference
CdSe NR	(*a*=1.7 nm, *l*=18 nm)-(*a*=3.5 nm, *l*=34 nm) **$5.3x10^{-15}$-$1.4x10^{-14}$**	(*a*=1.7 nm, *l*=18 nm)-(*a*=3.5 nm, *l*=34 nm) **$4.0x10^{-15}$-$3.0x10^{-14}$** @532 nm	19
	(*a*=1.8 nm, *l*=24 nm)-(*a*=2.5 nm, *l*=25 nm) **$7.6x10^{-15}$-$4.6x10^{-15}$**		20
CdSe NW	(*a*=3.0 nm, *l*=1 μm)-(*a*=21 nm, *l*=1μm) **$6.9x10^{-13}$-$3.9x10^{-11}$**	(*a*=3.0 nm, *l*=1 μm)-(*a*=21 nm, *l*=1μm) **$6.9x10^{-13}$-$3.9x10^{-11}$** @488 nm	21
CdTe NW	(*a*=3.8 nm, *l*=1 μm)-(*a*=6.0 nm, *l*=1 μm) **$4.3x10^{-13}$-$5.1x10^{-12}$**	(*a*=3.8 nm, *l*=1 μm)-(*a*=6.0 nm, *l*=1 μm) **$1.8x10^{-12}$-$2.0x10^{-11}$** @488 nm	21

3. Modeling the PHI signal

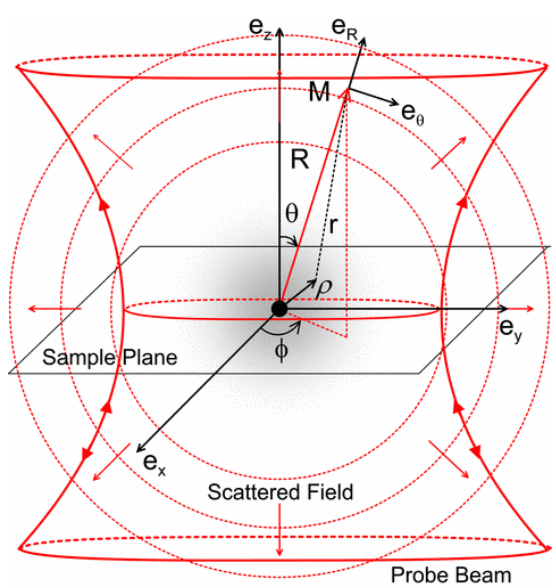

Figure S1. Illustration of the observation point M relative to the analyte (center dot). $\boldsymbol{e_r}$, $\boldsymbol{e_\theta}$, and $\boldsymbol{e_\phi}$ (not shown) [$\boldsymbol{e_x}$, $\boldsymbol{e_y}$, $\boldsymbol{e_z}$] are the orthonormal basis vectors associated with the spherical [Cartesian] coordinate system. The local heating of the surrounding medium is depicted through

grey shaded region. The incident probe beam approaches the particle from below in the cartoon. Reprinted figure with permission from Reference 22. Copyright 2006 by the American Physical Society.

To model the PHI signal, we follow the analysis first presented by Lounis and co-workers.[22] **Figure S1** provides a schematic of the coordinate system used in the subsequent modeling. In the analysis, the analyte first absorbs the intensity of a heating laser, which is modulated at a frequency, Ω. The corresponding (modulated) absorbed power, P_{abs}, is linked to the analyte's absorption cross section via $P_{abs} = \sigma I_{exc}$. Following relaxation/heat dissipation into the surrounding medium, its induced, time-modulated, thermal profile is[23]

$$\Delta T(t) = \frac{P_{abs}}{4\pi k\rho}\left[1 + e^{-\frac{\rho}{r_{th}}}\cos\left(\Omega t - \frac{\rho}{r_{th}}\right)\right] \tag{S6}$$

where $r_{th} = \sqrt{\frac{2D}{\Omega}}$ is a characteristic heat diffusion length with $D = \frac{\kappa}{C_p}$ the thermal diffusivity of the surrounding medium and κ (C_p) the medium's thermal conductivity (heat capacity per unit volume). What results is a change to the medium's susceptibility of the form $\Delta\chi = 2n_m\left(\frac{\partial n_m}{\partial T}\right)\Delta T$ where n_m is the medium's refractive index and with $\left(\frac{\partial n_m}{\partial T}\right)$ reflecting how sensitive n_m is to temperature changes.

Next, an incident, circularly polarized, probe field is assumed to be incident on the analyte and its immediate surroundings. The probe field is expressed as $\boldsymbol{E}_{probe}(\boldsymbol{\rho}, t) = E_o e^{i(\boldsymbol{k_i}\cdot\boldsymbol{\rho}-\omega t)}\boldsymbol{e}_+$ where $\boldsymbol{e}_+ = \frac{1}{\sqrt{2}}(\boldsymbol{e}_x + i\boldsymbol{e}_y)$. Its interaction with the medium's time-modulated susceptibility then yields an induced polarization[22,24]

$$\boldsymbol{P}(\boldsymbol{\rho}, t) = \frac{\varepsilon_o}{n_m^2}\Delta\chi\boldsymbol{E}_{probe}. \tag{S7}$$

At this point, what is ultimately desired is an expression for the scattered field, $\boldsymbol{E}_{\Omega}$, due to the time-modulated susceptibility exhibited by the local medium. This is done using the Hertz potential, $\mathbf{\Pi}$, via[22,24,25]

$$\mathbf{\Pi} = \frac{1}{4\pi\varepsilon_o}\int d^3\boldsymbol{\rho}\int dt'\,\frac{\boldsymbol{P}(\boldsymbol{\rho},t)\delta\left(t'-t+|\boldsymbol{R}-\boldsymbol{\rho}|/c_m\right)}{|\boldsymbol{R}-\boldsymbol{\rho}|}. \tag{S8}$$

Only time-dependent terms are kept during the evaluation of **Equation S8** since this is what is eventually monitored in the measurement as the heterodyned signal at Ω. Furthermore, $|\boldsymbol{R}-\boldsymbol{\rho}| \approx R$ is assumed in **Equation S8** since the detection in the far field is assumed to be a good distance away from the analyte. What results is

$$\mathbf{\Pi} = \frac{1}{4\pi\varepsilon_o}\left(\frac{\varepsilon_o}{n_m^2}\right)\left[2n_m\left(\frac{\partial n_m}{\partial T}\right)\right]\left[\frac{P_{abs}}{4\pi kR}\right]\left(\frac{E_o\boldsymbol{e}_+}{2}\right)\left[e^{i[k_sR-(\omega-\Omega)t]}\int\frac{d^3\boldsymbol{\rho}}{\rho}e^{-\frac{\rho}{r_{th}}+i\left(\boldsymbol{k_i}\cdot\boldsymbol{\rho}-\frac{\rho}{r_{th}}\right)}+\right.$$

$$\left.e^{i[k_sR-(\omega+\Omega)t]}\int\frac{d^3\boldsymbol{\rho}}{\rho}e^{-\frac{\rho}{r_{th}}+i\left(\boldsymbol{k_i}\cdot\boldsymbol{\rho}+\frac{\rho}{r_{th}}\right)}\right].$$

Letting $\boldsymbol{k_i} \rightarrow \Delta\boldsymbol{k} = (\boldsymbol{k}_i - \boldsymbol{k}_s) = \frac{2n_m\pi}{\lambda}(\boldsymbol{e_z} - \boldsymbol{e_R})$ and defining

$$I^- = \int\frac{d^3\boldsymbol{\rho}}{\rho}e^{-\frac{\rho}{r_{th}}+i\left(\Delta\boldsymbol{k}\cdot\boldsymbol{\rho}-\frac{\rho}{r_{th}}\right)} \tag{S9}$$

$$I^+ = \int\frac{d^3\boldsymbol{\rho}}{\rho}e^{-\frac{\rho}{r_{th}}+i\left(\Delta\boldsymbol{k}\cdot\boldsymbol{\rho}+\frac{\rho}{r_{th}}\right)} \tag{S10}$$

gives

$$\mathbf{\Pi} = \frac{1}{\varepsilon_o}\left[2n_m\left(\frac{\partial n_m}{\partial T}\right)\right]\left[\frac{P_{abs}}{(4\pi)^2kR}\right]\left(\frac{\varepsilon_o}{n_m^2}\right)\left[I^+e^{i[k_sR-(\omega+\Omega)t]}+I^-e^{i[k_sR-(\omega-\Omega)t]}\right]\left(\frac{E_o\boldsymbol{e}_+}{2}\right). \tag{S11}$$

I^+ and I^- are subsequently integrated with $d^3\boldsymbol{\rho} = \rho^2\sin\theta d\theta d\phi d\rho$, $\Delta\boldsymbol{k}\cdot\boldsymbol{\rho} = |\Delta\boldsymbol{k}|\rho\cos\theta$ and by ultimately making the substitution $u = |\Delta\boldsymbol{k}|r_{th}$. What results are the following explicit expressions

$$I^{\pm} = 2\pi r_{th}^2[f(\theta,\Omega) \mp ig(\theta,\Omega)] \tag{S12}$$

where

$$f(\theta,\Omega) = \frac{1}{u}\left(\frac{u+1}{(u+1)^2+1} + \frac{u-1}{(u-1)^2+1}\right) \tag{S13}$$

$$g(\theta,\Omega) = \frac{1}{u}\left(\frac{1}{(u+1)^2+1} - \frac{1}{(u-1)^2+1}\right). \tag{S14}$$

and where $u = |\Delta k| r_{th} = \frac{4n_m\pi}{\lambda}\sqrt{\frac{2D}{\Omega}}\sin\left(\frac{\theta}{2}\right)$.

The scattered probe field

The desired scattered probe electric field is found from[22,24]

$$\boldsymbol{E}_\Omega = \nabla_R \times (\nabla_R \times \boldsymbol{\Pi}) \tag{S15}$$

$$= \frac{1}{2\varepsilon_o}(\boldsymbol{E}^+ + \boldsymbol{E}^-)$$

where

$$\boldsymbol{E}^+ = \left[2n_m\left(\frac{\partial n_m}{\partial T}\right)\frac{P_{abs}}{(4\pi)^2 kR}\frac{\varepsilon_o}{n_m^2}\right]\nabla_R \times \left[\nabla_R \times \boldsymbol{e}_+ I^+ E_o e^{i[k_s R-(\omega+\Omega)t]}\right] \tag{S16}$$

$$\boldsymbol{E}^- = \left[2n_m\left(\frac{\partial n_m}{\partial T}\right)\frac{P_{abs}}{(4\pi)^2 kR}\frac{\varepsilon_o}{n_m^2}\right]\nabla_R \times \left[\nabla_R \times \boldsymbol{e}_+ I^- E_o e^{i[k_s R-(\omega-\Omega)t]}\right]. \tag{S17}$$

Subsequent simplification with ${r_{th}}^2 = \frac{2D}{\Omega}$ and $D = \frac{k}{C_p}$ gives

$$\boldsymbol{E}_\Omega = \frac{2\pi}{C_p}\left[n_m\left(\frac{\partial n_m}{\partial T}\right)\frac{P_{abs}}{(2n_m\pi)^2}\frac{E_o}{R}\left(\frac{1}{2\Omega}\right)\right]\left[\nabla_R \times \nabla_R \times \boldsymbol{a}e^{i[k_s R-\omega t]} + \nabla_R \times \nabla_R \times \boldsymbol{b}e^{i[k_s R-\omega t]}\right] \tag{S18}$$

with $\boldsymbol{a} = \boldsymbol{e}_+ I^{+\prime} e^{-i\Omega t}$, $\boldsymbol{b} = \boldsymbol{e}_+ I^{-\prime} e^{-i\Omega t}$, $I^{+\prime} = [f(\theta,\Omega) - ig(\theta,\Omega)]$, and $I^{-\prime} = [f(\theta,\Omega) + ig(\theta,\Omega)]$.

The double curl terms in **Equation S18** simplify using the identity $[\nabla \times (f\boldsymbol{A})] = f(\nabla \times \boldsymbol{A}) + (\nabla f) \times \boldsymbol{A}$ where *f* is a generic scalar function. Consequently, the first double curl evaluates as

$$\nabla_R \times \nabla_R \times \boldsymbol{a}e^{i[k_s R-\omega t]} = \nabla_R \times \left[\nabla_R \times \boldsymbol{a}e^{i[k_s R-\omega t]}\right]$$

$$= \nabla_R \times \left[e^{i[k_s R-\omega t]}(\nabla \times \boldsymbol{a}) + \left(\nabla e^{i[k_s R-\omega t]}\right) \times \boldsymbol{a}\right]$$

where $(\nabla \times \boldsymbol{a}) = 0$. Evaluating the gradient ($\nabla_R = \frac{\partial}{\partial r}\boldsymbol{e_R}$) then gives

$$\nabla_R \times \nabla_R \times \boldsymbol{a}e^{i[k_s R-\omega t]} = \nabla_R \times \left[\left(\nabla e^{i[k_s R-\omega t]}\right) \times \boldsymbol{a}\right]$$

$$= \nabla_R \times \left[ik_s e^{i[k_s R-\omega t]}(\boldsymbol{e_R} \times \boldsymbol{a})\right].$$

A second application of the identity yields

$$\nabla_R \times \nabla_R \times \boldsymbol{a}e^{i[k_s R-\omega t]} = ik_s e^{i[k_s R-\omega t]}\left(\nabla_R \times (\boldsymbol{e_R} \times \boldsymbol{a})\right) + \nabla_R\left(ik_s e^{i[k_s R-\omega t]}\right) \times (\boldsymbol{e_R} \times \boldsymbol{a})$$

with $\left(\nabla_R \times (\boldsymbol{e_R} \times \boldsymbol{a})\right)$=0. What remains is

$$\nabla_R \times \nabla_R \times \boldsymbol{a}e^{i[k_s R-\omega t]} = \nabla_R\left(ik_s e^{i[k_s R-\omega t]}\right) \times (\boldsymbol{e_R} \times \boldsymbol{a})$$

$$= (ik_s)^2 e^{i[k_s R-\omega t]}[\boldsymbol{e_R} \times (\boldsymbol{e_R} \times \boldsymbol{a})].$$

Since $k_s = \frac{2n_m\pi}{\lambda}$, one obtains

$$\nabla_R \times \nabla_R \times \boldsymbol{a}e^{i[k_s R-\omega t]} = -\left(\frac{2n_m\pi}{\lambda}\right)^2 e^{i[k_s R-\omega t]}[\boldsymbol{e_R} \times (\boldsymbol{e_R} \times \boldsymbol{a})].$$

Subsequent simplification gives

$$\nabla_R \times \nabla_R \times \boldsymbol{a}e^{i[k_s R-\omega t]} = -\left(\frac{2n_m\pi}{\lambda}\right)^2 I^{+\prime} e^{-i\Omega t} e^{i[k_s R-\omega t]}[\boldsymbol{e_R} \times (\boldsymbol{e_R} \times \boldsymbol{e}_+)]. \quad \text{(S19)}$$

The second double curl in **Equation S18** similarly becomes

$$\nabla_R \times \nabla_R \times \boldsymbol{b}e^{i[k_s R-\omega t]} = -\left(\frac{2n_m\pi}{\lambda}\right)^2 I^{-\prime} e^{i\Omega t} e^{i[k_s R-\omega t]}[\boldsymbol{e_R} \times (\boldsymbol{e_R} \times \boldsymbol{e}_+)]. \quad \text{(S20)}$$

With this, one obtains an expression for the scattered probe field, arising from the time-modulated susceptibility of the surrounding medium

$$\boldsymbol{E}_\Omega = -2\pi\left[n_m\left(\frac{\partial n_m}{\partial T}\right)\frac{P_{abs}}{C_p\lambda^2}\right]\left(\frac{E_o e^{i[k_s R-\omega t]}}{R}\right)\left[\frac{f(\theta,\Omega)\cos\Omega t - g(\theta,\Omega)\sin\Omega t}{\Omega}\right][\boldsymbol{e_R} \times (\boldsymbol{e_R} \times \boldsymbol{e}_+)]. \quad \text{(S21)}$$

Heterodyned signal

To obtain the heterodyned signal, E_o in **Equation S21** is expressed in terms of the electric field amplitude at the beam waist, w. Specifically, since the power at the beam waist is $P_{probe} = |E_o|^2(\pi w^2)$, $E_o = \frac{1}{w}\sqrt{\frac{P_{probe}}{\pi}}$ such that

$$\boldsymbol{E}_\Omega = -2\pi\left[n_m\left(\frac{\partial n_m}{\partial T}\right)\frac{P_{abs}}{wC_p\lambda^2}\right]\left[\frac{f(\theta,\Omega)\cos\Omega t - g(\theta,\Omega)\sin\Omega t}{\Omega}\right]\left[\sqrt{\frac{P_{probe}}{\pi}}\frac{e^{i(k_s R-\omega t)}}{R}\right][\boldsymbol{e_R} \times (\boldsymbol{e_R} \times \boldsymbol{e}_+)]. \quad \text{(S22)}$$

Next, the local oscillator, which stems from the reflected (or transmitted) probe beam, is assumed to take the form of a spherical wave in the far field.[22] Its specific form is

$$\boldsymbol{E}_{local} = -E_R e^{i(k_s R-\omega t)}[\boldsymbol{e_R} \times (\boldsymbol{e_R} \times \boldsymbol{\mu})] = -\frac{\beta}{R} e^{i(k_s R-\omega t)}[\boldsymbol{e_R} \times (\boldsymbol{e_R} \times \boldsymbol{\mu})]. \quad \text{(S23)}$$

where β is a constant to be determined and with a dipole origin for the local oscillator implicitly assumed.[26] This explains $[\boldsymbol{e_R} \times (\boldsymbol{e_R} \times \boldsymbol{\mu})]$ where $\boldsymbol{\mu}$ is the dipole moment and where $\boldsymbol{\mu} = \boldsymbol{e}_+$.

Since the power from the beam waist is the same as that projected onto the surface area of a hemisphere of radius R in either the forward and back-scattered geometries, $|E_o|^2(\pi w^2)$=$|E_R|^2(2\pi R^2)$ so that $E_R = \frac{\beta}{R} = \frac{w}{\sqrt{2}R}E_o$. Using $E_o = \frac{1}{w}\sqrt{\frac{P_{probe}}{\pi}}$ one then finds the following expression for the local oscillator in the far field

$$\boldsymbol{E}_{local} = -\sqrt{\frac{P_{probe}}{2\pi}}\frac{e^{i(k_s R-\omega t)}}{R}[\boldsymbol{e_R} \times (\boldsymbol{e_R} \times \boldsymbol{e}_+)]. \quad \text{(S24)}$$

The heterodyned signal, I_{hetero}, is obtained through the interference term of

$$I = |\boldsymbol{E}_\Omega + \boldsymbol{E}_{local}|^2 = |\boldsymbol{E}_\Omega|^2 + |\boldsymbol{E}_{local}|^2 + 2Re(\boldsymbol{E}_{local}{}^*\boldsymbol{E}_\Omega) \quad \text{(S25)}$$

and is

$$\begin{aligned} I_{hetero} &= 2Re(\boldsymbol{E}_{local}{}^*\boldsymbol{E}_\Omega) \\ &= \frac{2\sqrt{2}\sqrt{P_{probe}P_{probe}}}{wR^2}\left[n_m\left(\frac{\partial n_m}{\partial T}\right)\frac{P_{abs}}{C_p\lambda^2}\right]\left[\frac{f(\theta,\Omega)\cos\Omega t - g(\theta,\Omega)\sin\Omega t}{\Omega}\right]|\boldsymbol{e_R} \\ &\quad \times (\boldsymbol{e_R} \times \boldsymbol{e}_+)|^2. \end{aligned}$$

Since the differential solid angle and corresponding surface area are linked via $d\Omega = \frac{dA}{R^2}$, the differential power of the heterodyned signal is $\frac{dP_{hetero}}{d\Omega} = I_{hetero}R^2$. What results is

$$\frac{dP_{hetero}}{d\Omega} = \frac{2\sqrt{2}\sqrt{P_{probe}P_{probe}}}{w}\left[n_m\left(\frac{\partial n_m}{\partial T}\right)\frac{P_{abs}}{C_p\lambda^2}\right]\left[\frac{f(\theta,\Omega)\cos\Omega t - g(\theta,\Omega)\sin\Omega t}{\Omega}\right]|\boldsymbol{e_R} \times (\boldsymbol{e_R} \times \boldsymbol{e}_+)|^2 \quad \text{(S26)}$$

where $|\boldsymbol{e_R} \times (\boldsymbol{e_R} \times \boldsymbol{e}_+)|^2 = |\boldsymbol{e_R} \times \boldsymbol{e}_+|^2 = \frac{1}{2}[1 + \cos^2\theta]$. The resulting differential power per solid angle is

$$\frac{dP_{hetero}}{d\Omega} = \frac{\sqrt{2}\sqrt{P_{probe}P_{probe}}}{w}\left[n_m\left(\frac{\partial n_m}{\partial T}\right)\frac{P_{abs}}{C_p\lambda^2}\right]\left[\frac{f(\theta,\Omega)\cos\Omega t - g(\theta,\Omega)\sin\Omega t}{\Omega}\right][1 + \cos^2\theta]. \quad \text{(S27)}$$

Equation S27 is integrated, i.e. $P_{hetero} = \int\int \frac{dP_{hetero}}{d\Omega}\sin\theta d\theta d\phi$, to obtain

$$P_{hetero} = \frac{2\pi\sqrt{2}\sqrt{P_{probe}P_{probe}}}{w}\left[n_m\left(\frac{\partial n_m}{\partial T}\right)\frac{P_{abs}}{C_p\lambda^2}\right][F(\Omega)\cos\Omega t - G(\Omega)\sin\Omega t] \quad \text{(S28)}$$

where

$$F(\Omega) = \frac{1}{\Omega}\int_{\theta_{min}}^{\theta_{max}} f(\theta,\Omega)[1 + \cos^2\theta]\sin\theta d\theta \quad \text{(S29)}$$

$$G(\Omega) = \frac{1}{\Omega}\int_{\theta_{min}}^{\theta_{max}} g(\theta,\Omega)[1 + \cos^2\theta]\sin\theta d\theta. \quad \text{(S30)}$$

In the forward-transmission geometry, $\theta_{min} = 0$ and $\theta_{max} = \frac{\pi}{2}$ while in the back-reflection geometry $\theta_{min} = \frac{\pi}{2}$ and $\theta_{max} = \pi$.[22]

If transmission or reflection efficiency factors are included in **Equation S24** for $\boldsymbol{E}_{\text{local}}$, i.e. $P_{probe} \rightarrow \alpha P_{probe}$ where α is either the reflectivity or transmissivity of the sample/substrate and which depends on the experimental geometry, one obtains

$$P_{hetero} = \frac{2\pi\sqrt{2\alpha}P_{probe}}{w}\left[n_m\left(\frac{\partial n_m}{\partial T}\right)\frac{P_{abs}}{C_p\lambda^2}\right][F(\Omega)\cos\Omega t - G(\Omega)\sin\Omega t]. \quad \text{(S31)}$$

If desired, the transmissivity (η) of the optical path in either forward or backscattered geometries can also be accounted for by multiplying P_{hetero} with η.[22] However, for convenience, η will be assumed to equal 1. This is **Equation 5** of the main text.

4. Size-dependent Au NP extinction cross sections and Mie theory predictions

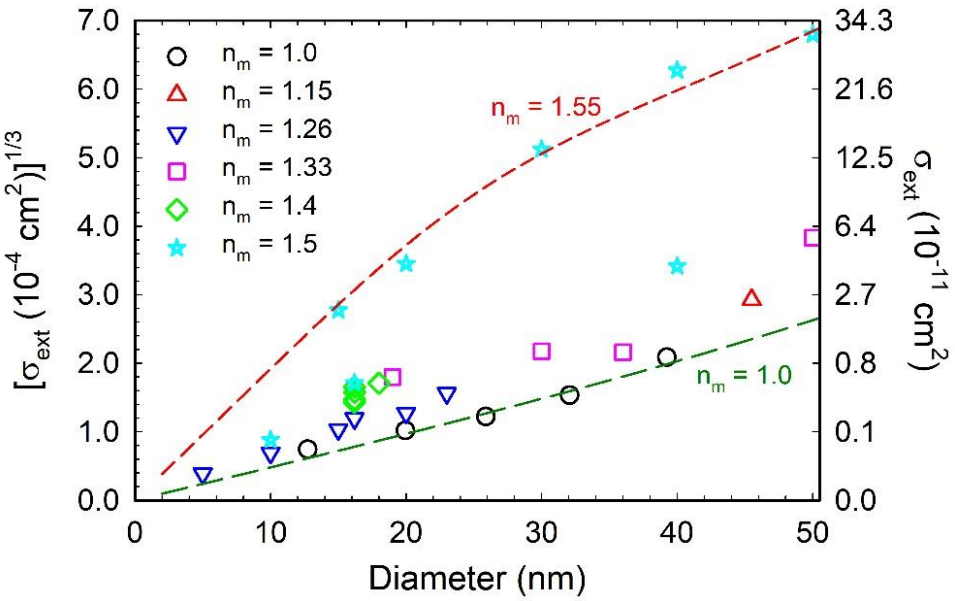

Figure S2. Mie theory Au NP extinction σ-values for surrounding medium refractive indices of n_m = 1.55 and 1.00 (dotted green and black dashed lines, respectively). Literature σ-values for different-sized Au NPs: ○ (n_m=1.00 [Reference 27]), △ (n_m=1.15 [Reference 28]), ▽ (n_m=1.26 [References 29, 30 and 31]), □ (n_m=1.33 [Reference 32]), ◊ (n_m=1.40 [References 30, 33, and 34]), ☆ (n_m=1.50 [References 30, 35, and 36]).

5. Conceptual illustration of SMS microscopy

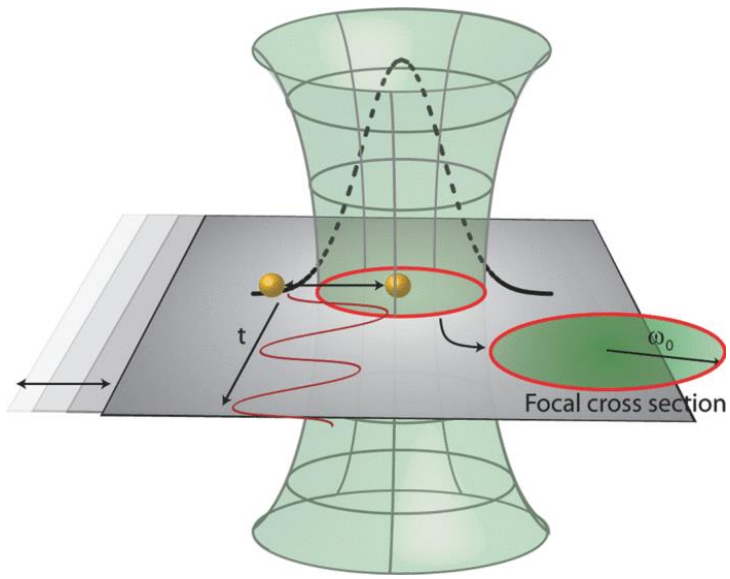

Figure S3. Cartoon representation of the laser focus and spatial modulation of the sample in the SMS experiment. Reprinted from Reference 27 with permission from AIP Publishing.

6. Modeling the SMS signal through a Taylor series expansion

$I_{exc}(x,y)$ in **Equation 11** of the main text is expanded as a Taylor series[29,37]

$$I_{exc}(x,y) \approx I_o\left[g + \left(\frac{\partial g}{\partial x}\right)(\Delta x) + \frac{1}{2}\left(\frac{\partial^2 g}{\partial x^2}\right)(\Delta x)^2 + \cdots\right] \tag{S32}$$

where $g = e^{-\frac{2[(x-x_o)^2-(y-y_o)^2]}{w^2}}$. Simplification yields

$$I(x,y,t) \approx \left(\frac{2P_o}{\pi w^2}\right)\left[\left(f + \frac{\delta^2}{4}\left(\frac{\partial^2 g}{\partial x^2}\right)\right) + \delta\left(\frac{\partial g}{\partial x}\right)(\sin\Omega t) - \frac{\delta^2}{4}\left(\frac{\partial^2 g}{\partial x^2}\right)(\cos 2\Omega t) + \cdots\right]$$

where the specific terms of interest are the 1*f* and 2*f* contributions of the expansion since they are ultimately sampled by the lock-in amplifier. Corresponding 1*f* and 2*f* intensities are

$$I_{1f}(x,y) = -\left(\frac{8P_o\delta}{\pi w^4}\right) x e^{-\frac{2[(x-x_o)^2-(y-y_o)^2]}{w^2}} \tag{S33}$$

$$I_{2f}(x,y) = -\left(\frac{2P_o\delta^2}{\pi w^4}\right)\left[\frac{4x^2}{w^2} - 1\right] e^{-\frac{2[(x-x_o)^2-(y-y_o)^2]}{w^2}}. \tag{S34}$$

with associated changes in transmitted power of $\Delta P_{1f/2f} = \left(P_o - P_{1f/2f}\right) = \sigma I_{1f/2f}$. Lock-in-reported AC voltages are found from

$$V_{AC,1f/2f} = R_{det} G_{det} \Delta P_{1f/2f} \tag{S35}$$

where R_{det} is the photodetector responsivity and G_{det} is its transimpedance gain. Experimental 1*f* and 2*f* AC outputs are therefore

$$V_{AC,1f}(x,y) = -\sigma\left(\frac{8P_o\delta}{\pi w^4}\right) x e^{-\frac{2(x^2+y^2)}{w^2}} \tag{S36a}$$

$$V_{AC,2f}(x,y) = -\sigma\left(\frac{2P_o\delta^2}{\pi w^4}\right)\left[\frac{4x^2}{w^2} - 1\right] e^{-\frac{2(x^2+y^2)}{w^2}}. \tag{S36b}$$

This is **Equation 14** of the main text. Simulated SMS images for **Equation 14** are shown in **Figure S4** below.

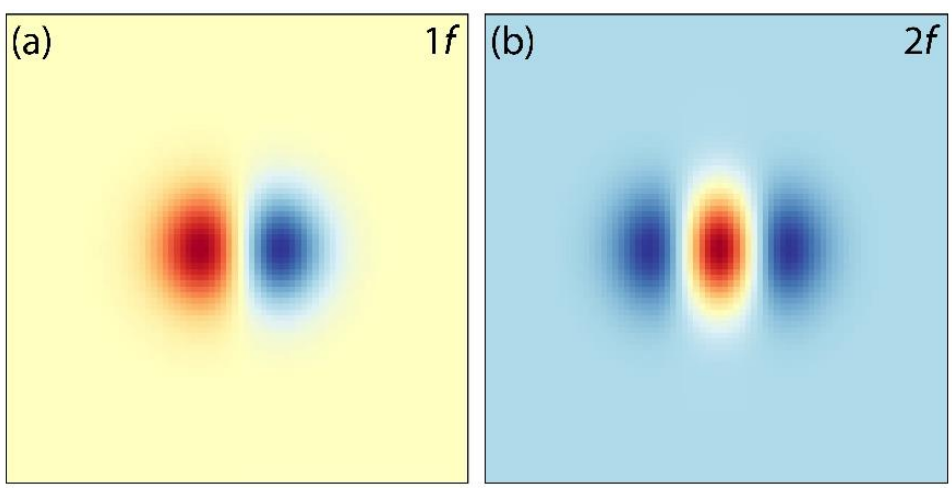

Figure S4. Simulated SMS images of a particle using (a) 1*f* and (b) 2*f* detection. Taylor series expressions used to generate the images.

7. Modeling the SMS signal through a Fourier series expansion

I_{exc} (**Equation 12** of the main text) is expanded using a Fourier series. To this end, the intensity profile is first expressed as

$$I_{exc}(x,y) = I_o f(x_p) e^{-\frac{2(y-y_o)^2}{w^2}}$$

where $f(x_p) = e^{-\frac{2(x_p)^2}{w^2}}$ with $x_p = (x + \delta \sin \Omega t) - x_o$. Next, the Fourier series expansion of $f(x_p)$ is given by

$$f_F(x_p) = \left[\frac{a_0}{2} + \sum_{n=1}^{\infty}[a_n \cos(n\Omega t) + b_n \sin(n\Omega t)]\right] \tag{S37}$$

where

$$a_0 = \frac{\Omega}{\pi}\int_{-\frac{\pi}{\Omega}}^{\frac{\pi}{\Omega}} f(x_p) dt \tag{S38}$$

$$a_n = \frac{\Omega}{\pi}\int_{-\frac{\pi}{\Omega}}^{\frac{\pi}{\Omega}} f(x_p) \cos(n\Omega t)\, dt \tag{S39}$$

$$b_n = \frac{\Omega}{\pi}\int_{-\frac{\pi}{\Omega}}^{\frac{\pi}{\Omega}} f(x_p) \sin(n\Omega t)\, dt. \tag{S40}$$

In **Equation S37**, odd values of *n* result in $a_n = 0$ while even values give $b_n = 0$.

The resulting transmitted intensity is therefore

$$I_{exc}(x,y,t) = I_o\left(\frac{a_0}{2} + b_1 \sin(\Omega t) + a_2 \cos(2\Omega t) + \cdots\right) e^{-\frac{2(y-y_o)^2}{w^2}}. \tag{S41}$$

An associated transmitted power is $P_{trans} = P_o - \sigma I_{exc}$ with a corresponding detector output voltage ($V_{det} = R_{det} G_{det} P_{trans}$) of

$$V_{det}(x,y,t) = R_{det} G_{det} P_0 \left[1 - \sigma \frac{2}{\pi w^2}\left(\frac{a_0}{2} + b_1 \sin(\Omega t) + a_2 \cos(2\Omega t) + \cdots\right)\right] e^{-\frac{2(y-y_o)^2}{w^2}}. \tag{S42}$$

V_{det} contains the following DC term (where $\sigma \ll \pi w^2$; This is **Equation 15** of the main text)

$$V_{DC}(x,y) = \left(R_{det} G_{det} P_0 - \sigma \frac{a_0}{\pi w^2}\right) e^{-\frac{2(y-y_o)^2}{w^2}} \cong R_{det} G_{det} P_0 e^{-\frac{2(y-y_o)^2}{w^2}} \tag{S43}$$

and AC components

$$V_{AC}(x,y,t) = \left[\sigma \frac{2R_{det}G_{det}P_0}{\pi w^2}(b_1 \sin(\Omega t) + a_2 \cos(2\Omega t) + \cdots)\right] e^{-\frac{2(y-y_O)^2}{w^2}}. \tag{S44}$$

Resulting 1f and 2f AC voltages outputted by the lock-in are

$$V_{AC,1f}(x,y) = \left(\sigma \frac{2R_{det}G_{det}P_0}{\pi w^2} b_1\right) e^{-\frac{2(y-y_O)^2}{w^2}} \tag{S45a}$$

$$V_{AC,2f}(x,y) = \left(\sigma \frac{2R_{det}G_{det}P_0}{\pi w^2} a_2\right) e^{-\frac{2(y-y_O)^2}{w^2}}. \tag{S45b}$$

This is **Equation 16** of the main text. Simulated SMS images for **Equation 16** are shown in **Figure S5** below.

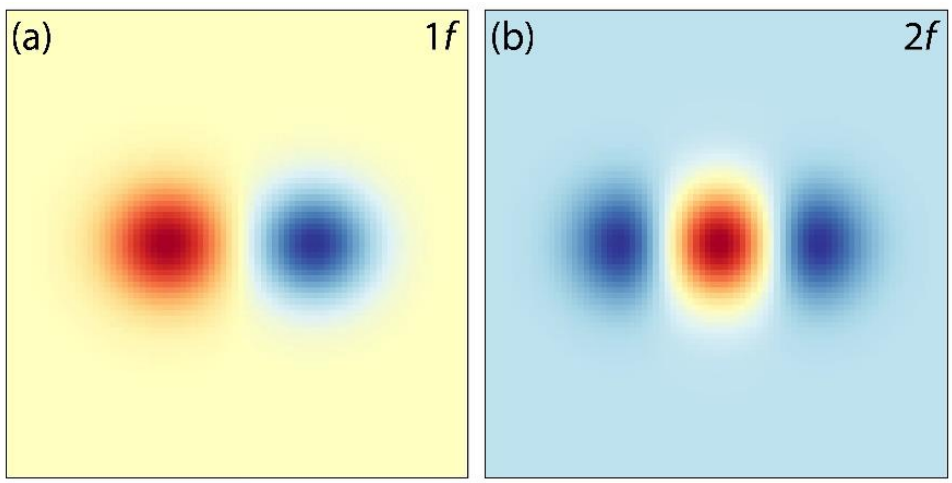

Figure S5. Simulated SMS images of a particle using (a) 1f and (b) 2f detection. Fourier series expressions used to generate the images.

8. SMS extinction spectra

The Fourier series approach readily produces expressions amenable to acquiring SMS spectra. Namely, to obtain extinction spectra, the analyte is brought to the origin and its position is modulated in x about x_o while keeping y constant at y=y_o. Since the 1f component [$b_1 \sin(\Omega t)$] in **Equation S44** is sinusoidal, its 1f RMS amplitude is $b_1/\sqrt{2}$. Consequently,

$$\frac{V_{lockin,RMS}^{1f}}{V_{DC}} = \frac{\sqrt{2}b_1}{\pi w^2}\sigma$$

where $V_{lockin,RMS}^{1f} \propto V_{AC,1f}$. Likewise, for the $2f$ component $[a_2 \cos(2\Omega t)]$

$$\frac{V_{lockin,RMS}^{2f}}{V_{DC}} = \frac{\sqrt{2}a_2}{\pi w^2}\sigma$$

with $V_{lockin,RMS}^{2f} \propto V_{AC,2f}$.

By using the lock-in to read only the $1f$ signal, specifically its maximum RMS reading, $V_{lockin,RMS}^{1f}(x_{max})$, one finds that the analyte's absorption cross section at a given excitation frequency/wavelength is

$$\sigma(\omega) = \frac{V_{lockin,RMS}^{1f}(x_{max})\pi w^2}{\sqrt{2}V_{DC}b_1}. \tag{S46}$$

This is **Equation 18** of the main text. In practice, x_{max} is determined empirically by stepping the particle through the laser focus. A corresponding excitation frequency/wavelength-dependent cross section, using the $2f$ RMS signal $[V_{lockin,RMS}^{2f}(x_{max})]$, is

$$\sigma(\omega) = \frac{V_{lockin,RMS}^{2f}(x_{max})\pi w^2}{\sqrt{2}V_{DC}a_2}. \tag{S47}$$

9. Custom autobalanced photodetector

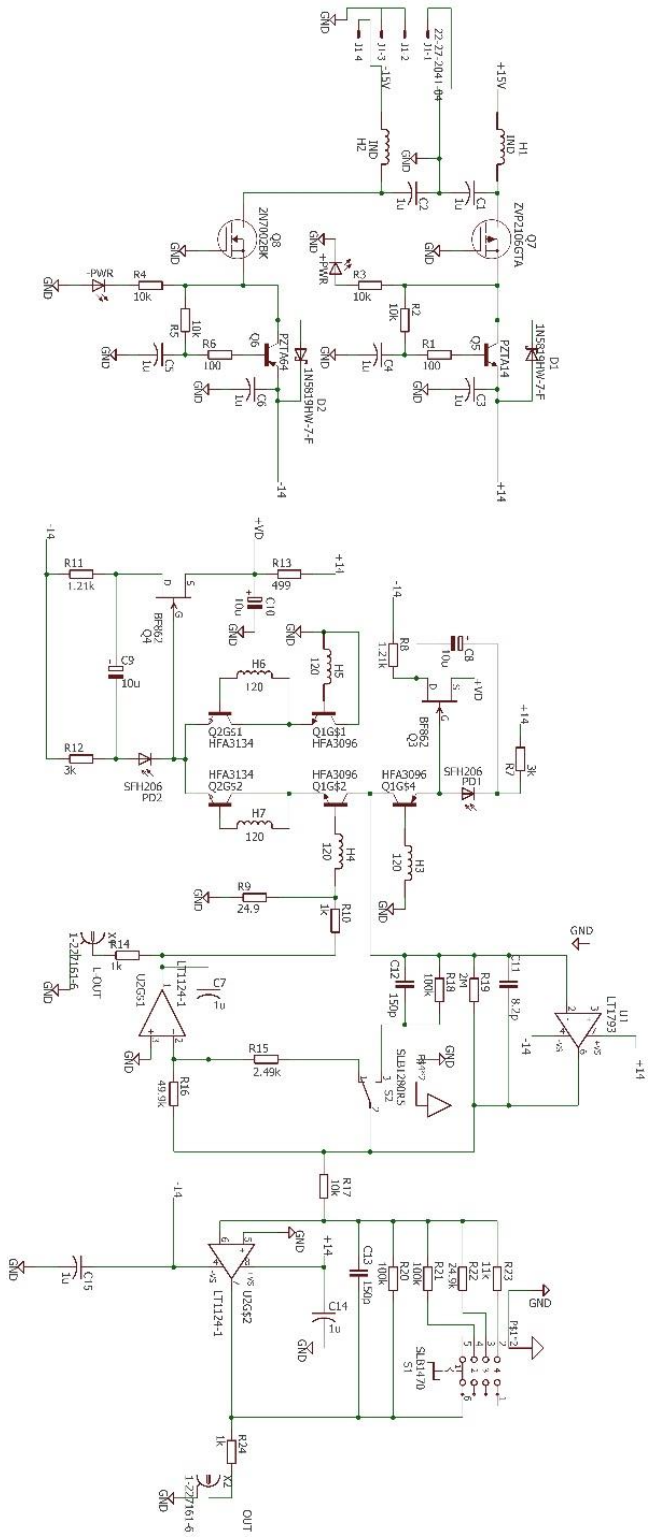

Figure S6. Circuit diagram of a custom autobalanced photodiode.

Table S3. Parts list for custom autobalanced photodetector.

Part	Value	Device	Package
C1	1 μF	10% 50V X7R capacitor	1206
C2	1 μF	10% 50V X7R capacitor	1206
C3	1 μF	10% 50V X7R capacitor	1206
C4	1 μF	10% 50V X7R capacitor	1206
C5	1 μF	10% 50V X7R capacitor	1206
C6	1 μF	10% 50V X7R capacitor	1206
C7	1 μF	10% 50V X7R capacitor	1206
C8	10 μF	10 % 35 V tantalum capacitor	D/7343-31R
C9	10 μF	10 % 35 V tantalum capacitor	D/7343-31R
C10	10 μF	10 % 35 V tantalum capacitor	D/7343-31R
C11	8.2 pF	5 % 50V NP0 capacitor	0805
C12	150 pF	5 % 50V NP0 capacitor	0805
C13	150 pF	5 % 50V NP0 capacitor	0805
C14	1 μF	10% 50V X7R capacitor	1206
C15	1 μF	10% 50V X7R capacitor	1206
D1	-	1N5819HW-7-F	SOD123
D2	-	1N5819HW-7-F	SOD123
H1	1 kΩ	BLM21AG102SN1D	0805
H2	1 kΩ	BLM21AG102SN1D	0805
H3	120 Ω	BLM21PG121SN1D	0805
H4	120 Ω	BLM21PG121SN1D	0805
H5	120 Ω	BLM21PG121SN1D	0805
H6	120 Ω	BLM21PG121SN1D	0805
H7	120 Ω	BLM21PG121SN1D	0805
J1	-	Connector	22-27-2041-04
PD1	-	SFH206	-
PD2	-	SFH206	-
Q1	-	HFA3096	SO16
Q2	-	HFA3134	SOT-23-6
Q3	-	BF862	SOT-23
Q4	-	BF862	SOT-23
Q5	-	PZTA14	SO223
Q6	-	PZTA64	SO223
Q7	-	ZVP2106GTA	SOT223
Q8	-	2N7002BK	SOT23-BEC
R1	100 Ω	1%	0805
R2	10 kΩ	1%	0805
R3	10 kΩ	1%	0805
R4	10 kΩ	1%	0805
R5	10 kΩ	1%	0805
R6	100 Ω	1%	0805

R7	3 kΩ	1%	0805
R8	1.21 kΩ	1%	0805
R9	24.9 Ω	1%	0805
R10	1 kΩ	1%	0805
R11	1.21 kΩ	1%	0805
R12	3 kΩ	1%	0805
R13	499 Ω	1%	0805
R14	1 kΩ	1%	0805
R15	2.49 kΩ	1%	0805
R16	49.9 kΩ	1%	0805
R17	10 kΩ	1%	0805
R18	100 kΩ	1%	0805
R19	2 MΩ	1%	0805
R20	100 kΩ	1%	0805
R21	100 kΩ	1%	0805
R22	24.9 kΩ	1%	0805
R23	11 kΩ	1%	0805
R24	1 kΩ	1%	0805
S1	-	SLB1470	-
S2	-	SLB1280R5	-
U1	-	LT1793	SO8
U2	-	LT1124-1	SO8
X1	-	1-227161-6	-
X2	-	1-227161-6	-

Noise comparison to Nirvana 2007

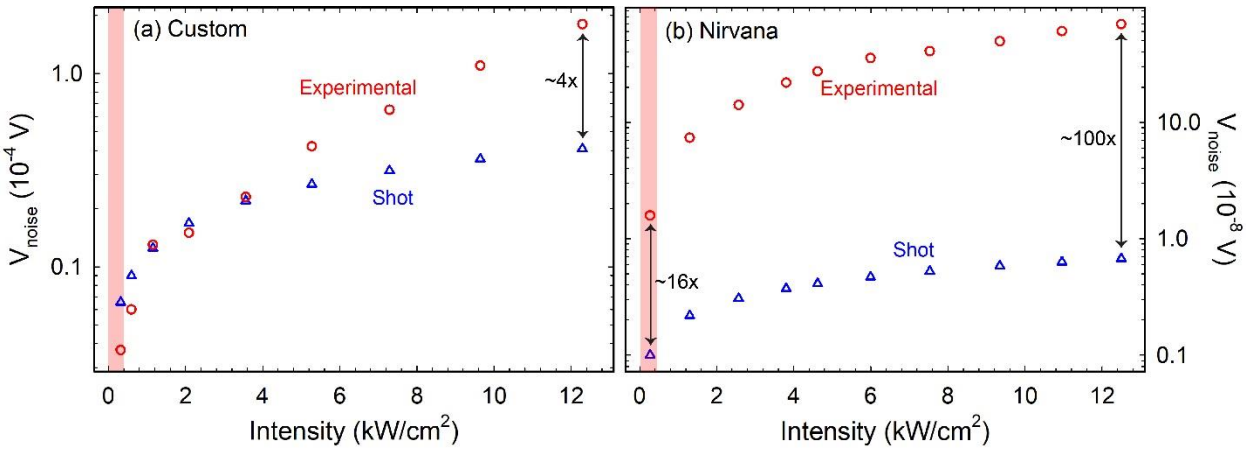

Figure S7. Experimental noise performance of (a) custom and (b) commercial autobalanced photodiodes. In either case, the calculated shot noise floor[27] is shown. Shaded red I_{exc} regions indicate where experiments have been conducted.

References

(1) Maxwell Garnett, J. C. Colours in Metal Glasses and in Metallic Films. *Philos. Trans. R. Soc. London* **1904**, *A203*, 385-420.

(2) Maxwell Garnett, J. C. Colours in Metal Glasses, in Metallic Films, and in Metallic Solutions II. *Philos. Trans. R. Soc. London* **1906**, *A205*, 237-288.

(3) Qin, L.; Li, D.; Zhang, Z.; Wang, K.; Ding, H.; Xie, R.; Yanga, W. The Determination of Extinction Coefficient of $CuInS_2$, and $ZnCuInS_3$ Multinary Nanocrystals. *Nanoscale* **2012**, *4*, 6360-6364.

(4) Shim, M.; Guyot-Sionnest, P. Permanent Dipole Moment and Charges in Colloidal Semiconductor Quantum Dots. *J. Chem. Phys.* **1999**, *111*, 6955-6964.

(5) Vossmeyer, T.; Katsikas, L.; Giersig, M.; Popovic, I. G.; Diesner, K.; Chemseddine, A.; Eychmuller, A.; Weller, H. CdS Nanoclusters - Synthesis, Characterization, Size-Dependent

Oscillator Strength, Temperature Shift of the Excitonic-Transition Energy, and Reversible Absorbency Shift. *J. Phys. Chem.* **1994**, *98*, 7665-7673.

(6) Yu, W. W.; Qu, L. H.; Guo, W. Z.; Peng, X. G. Experimental Determination of the Extinction Coefficient of CdTe, CdSe, and CdS Nanocrystals. *Chem. Mat.* **2003**, *15*, 2854-2860.

(7) Gong, K.; Kelley, D. F.; Kelley, A. M. Resonance Raman Excitation Profiles of CdS in Pure CdS and CdSe/CdS Core/Shell Quantum Dots: CdS-Localized Excitons. *J. Chem. Phys.* **2017**, *147*, 224702-224709.

(8) Hamachi, L. S.; Plante, I. J.-L.; Coryell, A. C.; De Roo, J.; Owen, J. S. Kinetic Control Over CdS Nanocrystal Nucleation Using a Library of Thiocarbonates, Thiocarbamates, and Thioureas. *Chem. Mater.* **2017**, *29*, 8711-8719.

(9) Ravi, V. K.; Swarnkar, A.; Chakraborty, R.; Nag, A. Excellent Green but Less Impressive Blue Luminescence from $CsPbBr_3$ Perovskite Nanocubes and Nanoplatelets. *Nanotechnology* **2016**, *27*, 325708.

(10) Schmelz, O.; Mews, A.; Basche, T.; Herrmann, A.; Mullen, K. Supramolecular Complexes from CdSe Nanocrystals and Organic Fluorophores. *Langmuir* **2001**, *17*, 2861-2865.

(11) Striolo, A.; Ward, J.; Prausnitz, J. M.; Parak, W. J.; Zanchet, D.; Gerion, D.; Milliron, D.; Alivisatos, A. P. Molecular Weight, Osmotic Second Virial Coefficient, and Extinction Coefficient of Colloidal CdSe Nanocrystals. *J. Phys. Chem. B* **2002**, *106*, 5500-5505.

(12) Leatherdale, C. A.; Woo, W. K.; Mikulec, F. V.; Bawendi, M. G. On the Absorption Cross Section of CdSe Nanocrystal Quantum Dots. *J. Phys. Chem. B* **2002**, *106*, 7619-7622.

(13) Jasieniak, J.; Smith, L.; van Embden, J.; Mulvaney, P. Re-examination of the Size-Dependent Absorption Properties of CdSe Quantum Dots. *J. Phys. Chem. C* **2009**, *113*, 19468-19474.

(14) Donega, C. d. M.; Koole, R. Size Dependence of the Spontaneous Emission Rate and Absorption Cross Section of CdSe and CdTe Quantum Dots. *J. Phys. Chem. C* **2009**, *113*, 6511-6520.

(15) Rajh, T.; Micic, O. I.; Nozik, A. J. Synthesis and Characterization of Surface-Modified Colloidal CdTe Quantum Dots. *J. Phys. Chem.* **1993**, *97*, 11999-12003.

(16) Yu, P. R.; Beard, M. C.; Ellingson, R. J.; Ferrere, S.; Curtis, C.; Drexler, J.; Luiszer, F.; Nozik, A. J. Absorption Cross-Section and Related Optical Properties of Colloidal InAs Quantum Dots. *J. Phys. Chem. B* **2005**, *109*, 7084-7087.

(17) Cademartiri, L.; Montanari, E.; Calestani, G.; Migliori, A.; Guagliardi, A.; Ozin, G. A. Size-Dependent Extinction Coefficients of PbS Quantum Dots. *J. Am. Chem. Soc.* **2006**, *128*, 10337-10346.

(18) Dai, Q.; Wang, Y.; Li, X.; Zhang, Y.; Pellegrino, D. J.; Zhao, M.; Zou, B.; Seo, J.; Wang, Y.; Yu, W. W. Size-Dependent Composition and Molar Extinction Coefficient of PbSe Semiconductor Nanocrystals. *ACS Nano* **2009**, *3*, 1518-1524.

(19) Wang, S.; Querner, C.; Emmons, T.; Drndic, M.; Crouch, C. H. Fluorescence Blinking Statistics from CdSe Core and Core/Shell Nanorods. *J. Phys. Chem. B* **2006**, *110*, 23221-23227.

(20) Shaviv, E.; Salant, A.; Banin, U. Size Dependence of Molar Absorption Coefficients of CdSe Semiconductor Quantum Rods. *Chem. Phys. Chem.* **2009**, *10*, 1028-1031.

(21) Protasenko, V.; Bacinello, D.; Kuno, M. Experimental Determination of the Absorption Cross Section and Molar Extinction Coefficient of CdSe and CdTe Nanowires. *J. Phys. Chem. B* **2006**, *110*, 25322-25331.

(22) Berciaud, S.; Lasne, D.; Blab, G. A.; Cognet, L.; Lounis, B. Photothermal Heterodyne Imaging of Individual Metallic Nanoparticles: Theory Versus Experiment. *Phys. Rev. B* **2006**, *73*, 045424.

(23) Carslaw, H. S.; Jaeger, J. C. *Conduction of Heat in Solids*; Oxford University Press: Oxford, UK, 1959.

(24) Chu, B. *Laser Light Scattering*; Academic Press: New York, NY, 1974.

(25) Lastovka, J. B. *Light Mixing Spectroscopy and the Spectrum of Light Scattered by Thermal Fluctuations in Liquids*; MIT PhD thesis, 1967.

(26) Gaiduk, A.; Ruijgrok, P. V.; Yorulmaz, M.; Orrit, M. Detection Limits in Photothermal Microscopy. *Chem. Sci.* **2010**, *1*, 343-350.

(27) McDonald, M. P.; Vietmeyer, F.; Aleksiuk, D.; Kuno, M. Supercontinuum Spatial Modulation Spectroscopy: Detection and Noise Limitations. *Rev. Sci. Instrum.* **2013**, *84*, 113104.

(28) Billaud, P.; Marhaba, S.; Cottancin, E.; Arnaud, L.; Bachelier, G.; Bonnet, C.; Del Fatti, N.; Lermé, J.; Vallée, F.; Vialle, J.-L.; et al. Correlation Between the Extinction Spectrum of a Single Metal Nanoparticle and its Electron Microscopy Image. *J. Phys. Chem. C* **2008**, *112*, 978-982.

(29) Arbouet, A.; Christofilos, D.; Del Fatti, N.; Vallée, F.; Huntzinger, J. R.; Arnaud, L.; Billaud, P.; Broyer, M. Direct Measurement of the Single-Metal-Cluster Optical Absorption. *Phys. Rev. Lett.* **2004**, *93*, 127401.

(30) Muskens, O. L.; Billaud, P.; Broyer, M.; Del Fatti, N.; Vallée, F. Optical Extinction Spectrum of a Single Metal Nanoparticle: Quantitative Characterization of a Particle and of its Local Environment. *Phys. Rev. B* **2008**, *78*, 205410.

(31) Devadas, M. S.; Li, Z. M.; Major, T. A.; Lo, S. S.; Havard, N.; Yu, K.; Johns, P.; Hartland, G. V. Detection of Single Gold Nanoparticles Using Spatial Modulation Spectroscopy Implemented with a Galvo-Scanning Mirror System. *Appl. Opt.* **2013**, *52*, 7806-7811.

(32) Devadas, M. S.; Li, Z.; Hartland, G. V. Imaging and Analysis of Single Optically Trapped Gold Nanoparticles Using Spatial Modulation Spectroscopy. *J. Phys. Chem. Lett.* **2014**, *5*, 2910-2915.

(33) Muskens, O. L.; Del Fatti, N.; Vallée, F. Single Metal Nanoparticle Absorption Spectroscopy and Optical Characterization. *Appl. Phys. Lett.* **2006**, *88*, 063109.

(34) Baida, H.; Christofilos, D.; Maioli, P.; Crut, A.; Del Fatti, N.; Vallée, F. Surface Plasmon Resonance Spectroscopy of Single Surfactant-Stabilized Gold Nanoparticles. *Eur. Phys. J. D* **2011**, *63*, 293-299.

(35) Payne, L.; Langbein, W.; Borri, P. Polarization-Resolved Extinction and Scattering Cross-Sections of Individual Gold Nanoparticles Measured by Wide-Field Microscopy on a Large Ensemble. *Appl. Phys. Lett.* **2013**, *102*, 131107.

(36) Payne, L.; Zoriniants, G.; Masia, F.; Arkill, K. P.; Verkade, P.; Rowles, D.; Langbein, W.; Borri, P. Optical Micro-Spectroscopy of Single Metallic Nanoparticles: Quantitative Extinction and Transient Resonant Four-Wave Mixing. *Faraday Discuss.* **2015**, *184*, 305-320.

(37) Devkota, T.; Devadas, M. S.; Brown, A.; Talghader, J.; Hartland, G. V. Spatial Modulation Spectroscopy Imaging of Nano-Objects of Different Sizes and Shapes. *Appl. Opt.* **2016**, *55*, 796-801.